MULTIPLE TEMPLATE DEFORMATION APPLICATION TO ABDOMINAL ORGAN SEGMENTATION

Romane Gauriau[⋆†], *Roberto Ardon*[⋆], *David Lesage*[⋆], *Isabelle Bloch*[†]

[⋆]Medisys Research Lab, Philips Research, Suresnes, France
[†]Institut Mines-Telecom, Telecom ParisTech, CNRS LTCI, Paris, France

ABSTRACT

We propose a fast, automatic and versatile framework for the segmentation of multiple anatomical structures from 2D and 3D images. We extend the work of [1] on implicit template deformation to multiple targets. Our variational formulation optimizes the non-rigid transformation of a set of templates according to image-driven forces. It embeds non-overlapping constraints ensuring a consistent segmentation result. We demonstrate the potential of our approach on the segmentation of abdominal organs (liver, kidneys, spleen and gallbladder) with an evaluation on CT volumes (50 for training and 50 for testing). Our method reaches state-of-the-art accuracy, ranging from 2mm (liver and kidneys) to 8mm (gallbladder).

Index Terms— Multi-organ segmentation, template deformation, automatic segmentation

1. INTRODUCTION

Segmentation is a key preliminary step in many medical applications such as planning and follow-up procedures, where modeling patients' organs is helpful for both visualization and quantitative measurements. Manually segmenting numerous organs is particularly tedious on large 3D acquisitions, emphasizing the need for automatic, fast and reliable algorithms.

Numerous works have been dedicated to single organ segmentation, but their generalization to multiple organs is often not straightforward. Despite refinements such as probabilistic and multi-atlases, atlas-based methods remain computationally expensive (e.g. $\sim$ 1h in [2]) and not always well-adapted to acute pathological cases. Among faster, recent alternatives, one can cite the work of [3] which proposes a level-set framework with inter-organs constraints (e.g. preventing overlap). It performs a fully automatic segmentation of several organs within a few minutes but relies on a large amount of training data (more than 300 datasets for the liver) and seemingly complex parameter tuning. Authors of [4] propose a very fast method (a few seconds) using landmarks regression and surface deformation based on discriminative classifiers. Authors show robust results on MR and CT data, but the required landmark definition remains a complex task which may hinder reproducibility and applicability to organs with large shape variations. Despite recent variants such as [5], classification-based approaches usually have difficulties enforcing spatial coherence and high contour accuracy so that additional regularization and refinement steps are often necessary.

This work was supported in part by an ANRT grant (008512012).

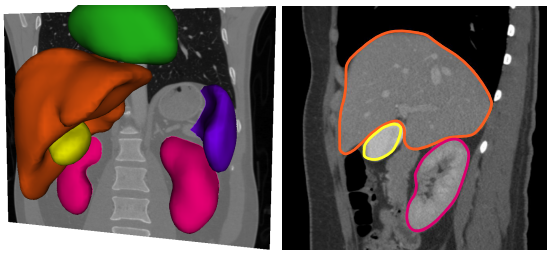

Fig. 1. Results of fine segmentation given by our method on two CT images, 3D rendering on the left and sagittal slice on the right (liver, kidneys, spleen, gallbaldder and heart).

Our framework offers a compelling tradeoff between accuracy, computational efficiency and simplicity. It is fully automatic, fast (less than 1min), flexible (multiple targets, 2D or 3D, easily tunable) and reaches state-of-the-art-level accuracy. First, Random Forest regressors with shape priors [6] provide us with *confidence maps* for the target organs (Sec. 2.1 and Fig. 2). These regressors are trained from a relatively limited amount of manually annotated data (in our case, 50 CT volumes). The confidence maps serve as inputs for a subsequent optimization, which constitutes the main contribution of this paper. We extend the work of [1] on implicit template deformation to multiple objects. Organ maps/templates are deformed jointly by composing individual poses with a single, shared non-rigid deformation field. Our variational framework relies on contrast-invariant region- and edge-based image forces. A key feature is the introduction of specific constraints preventing organ overlapping. Our approach balances the robustness of atlas-based methods with the adaptivity of active contour techniques. It leverages the efficiency of implicit template deformation [1] and extends it to multiple objects for a limited computational overhead. We demonstrate its potential on the segmentation of abdominal organs from CT volumes (Sec. 3 and Fig. 1). Finally we give an overview of the various perspectives of this work (Sec. 4).

978-1-4799-2374-8/15/$31.00 ©2015 IEEE

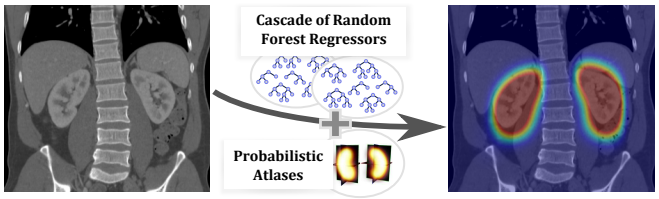

Fig. 2. Random forest localization, illustrated for the two kidneys (confidence maps overlayed on the right image).

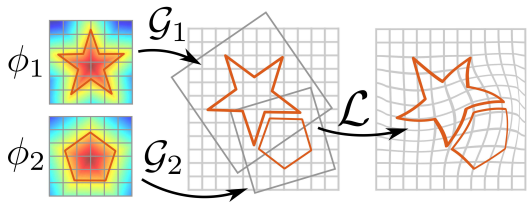

Fig. 3. Deformation scheme with two templates. The models ϕ_1 and ϕ_2 are globally transformed through transformations $\mathcal{G}_1$ and $\mathcal{G}_2$, where the non-overlapping constraint is applied, and then locally deformed through local deformation $\mathcal{L}$.

2. METHOD

We present our generic framework for the automatic segmentation of multiple objects. Automatic organ localization is done following the method of [6]. Segmentation is based on the generalization of implicit template deformation [7] to multiple models, which is the main contribution of this paper.

2.1. Multi-Organ Localization

Organ localization is performed in an automatic, fast and robust fashion thanks to a cascade of regression random forests with shape priors, as detailed in [6]. This approach provides us with *confidence maps* for each organ (see Fig.2), combining inter-patient variability (through shape priors) and data-specific uncertainty (through forest evaluation). Each map gives the chance of a voxel of the image to belong to a given organ. They are used to initialize subsequent segmentation steps and to attenuate image-driven forces. Notice that this step does not guarantee non overlapping between organs.

2.2. Multi-Objects Template Deformation Framework

2.2.1. *Implicit Deformation with Multiple Templates*

We denote an image $I : \Omega \to \mathbb{R}$ where $\Omega \in \mathbb{R}^d$ is the image domain ($d = 2$ or 3). For N target objects indexed by $n \in [\![1, N]\!]$, we define associated implicit shape templates $\phi_n : \Omega_n \to \mathbb{R}$ where Ω_n are the template referentials. These shape templates can be for instance probabilistic atlases. In our case, we can use directly the confidence maps given by the localization step (thus giving a patient-specific model). We define the transformations $\psi_n = \mathcal{G}_n \circ \mathcal{L}$ which acts on object n, where $\mathcal{G}_n : \Omega \to \Omega_n$ corresponds to the pose of object n (e.g. rigid or similarity transformation) and $\mathcal{L} : \Omega \to \Omega$ corresponds to the local deformation common to the set of templates in the domain Ω (see Fig. 3).

Our framework aims at optimizing the transformations $\psi_n : \Omega \to \Omega_n$ under image-derived forces f_n and regularity constraints on $\mathcal{L}$. The energy $E = E[\psi_1(\cdot), ..., \psi_N(\cdot)]$ to minimize is then defined as:

$$E = \sum_{n=1}^{N} \left(\int_{\Omega} H(\phi_n \circ \psi_n(x)).f_n(x)dx \right) + \frac{\lambda}{2}\|\mathcal{L} - Id\|_U^2 \tag{1}$$

where H is the Heaviside function and λ is a constant balancing data and regularization terms. The latter penalizes high amplitude deformations and thus controls the shape prior.

As in [1] we model the local transformation $\mathcal{L}$ as $\mathcal{L} = \mathbf{Id} + \mathbf{u}$. We follow the recent formulation of [8] defining the displacement field u in a kernel Hilbert space generated by a Gaussian kernel. Doing so ensures that $\mathcal{L}$ is a diffeomorphic transformation (Sec. 2.3).

2.2.2. *Non-Overlapping Constraint*

Equation 1 does not prevent overlapping between objects. Therefore we introduce non-overlapping constraints $C_{i,j}$, integrated as follows:

$$\begin{aligned} &\min_{\mathcal{G}_1,..\mathcal{G}_N,L} E(\mathcal{G}_1, .., \mathcal{G}_N, \mathcal{L}) \\ &\text{s. t. } \forall (i,j) \in [\![1, N]\!]^2, i < j, \\ &C_{i,j} = \int_{\Omega} H(\phi_i \circ \mathcal{G}_i(x)) H(\phi_j \circ \mathcal{G}_j(x)) dx = 0 \end{aligned} \tag{2}$$

These constraints apply on the models transformed by the pose transformations $\mathcal{G}_n$. The deformation $\mathcal{L}$, common to all objects, is diffeomorphic and thus prevents overlapping.

2.2.3. *Image-Derived Forces f_n*

The image-derived forces $f_n : \Omega \to \mathbb{R}$ drive the segmentation. They may be specific to each object n. This makes the framework flexible, easily tunable towards modality- or organ-specific information. In this paper, we define this term as a combination of a non parametric region term r_n and an edge term e_n such that $f_n(x) = \alpha r_n(x) + (1-\alpha) e_n(x)$ where α is a constant in $[0, 1]$. The region term is given by:

$$r_n(x) = \frac{p_{in}(I(x)) - p_{out}(I(x))}{p_{in}(I(x)) + p_{out}(I(x))}$$

where p_{in} and p_{out} are the intensity distributions inside and outside the n^{th} object estimated on the image I. The edge term e_n proposed in [9] is based on the Haralick edge detector. It relies on the second image derivatives computed in the direction orthogonal to the image level sets, thus guaranteeing

the alignment of the edges and the isolines of the image. To make this term contrast-invariant and object-dependent, the authors weight this term with the sign of the projection of the image gradient on the normal $\vec{n}$ to the object surface. Since $\vec{n} = \frac{\vec{\nabla}\phi}{\|\vec{\nabla}\phi\|}$, we generalize it to 3D as follows:

$$e_n(x) = \text{sign}\langle\vec{\nabla}I(x), \frac{\vec{\nabla}\phi}{\|\vec{\nabla}\phi\|}\rangle.\big(\Delta I(x) - \|\vec{\nabla}I(x)\|\text{div}\left(\frac{\vec{\nabla}I(x)}{\|\vec{\nabla}I(x)\|}\right)\big)$$

The forces $f_n(x)$ can be adapted to take into account the relationships between organs. The forces can be modulated by using the confidence maps given by the localization step. If M_k is a confidence map of the neighbor object k of object n which has K neighbors, the force term can be defined as:

$$f_n(x) = \left(\prod_{k=1}^{K} 1 - M_k(x)\right).(\alpha r_n(x) + (1-\alpha)e_n(x)) \quad (3)$$

The force term could also be the output of a discriminative classifier (as in [10]), at the cost of additional offline learning.

2.3. Numerical Optimization Scheme

We use the penalty method to turn Eq. 2 into a series of unconstrained minimizations:

$$\min_{\mathcal{G}_1,..,\mathcal{G}_N,L} \hat{E}_k \text{ with } \hat{E}_k = E + \frac{\mu_k}{2} \sum_{\substack{1\le i\le N \\ i<j\le N}} C_{i,j}^2 \quad (4)$$

where μ_k is the penalty coefficient. At each iteration k, μ_k is increased, the unconstrained problem is solved by gradient descent and used as the initialization for the next iteration.

The parametric transformations $\mathcal{G}_n$ are defined by N_g parameters $\mathbf{p_n} = \{p_{n,l}\}_{l=1...N_g}$ (e.g. $N_g = 6$ if $\mathcal{G}_n$ is rigid in $\mathbb{R}^3$). We assume that forces f_n are fixed during optimization. The minimization of Eq. 4 is done by gradient descent with composition update, since it guarantees a diffeomorphic transformation [8]. Starting from an initialization, $p_{n,l}$ and $\mathbf{u}$ are updated jointly and iteratively:

$$p_{n,l(t+1)} \leftarrow p_{n,l(t)} - \Delta t_p \frac{\partial \hat{E}_k}{\partial p_{n,l}}$$

$$\mathbf{u}_{(t+1)} \leftarrow \mathbf{u}_{(t)} \circ (\mathbf{Id} - \Delta t_u \vec{\nabla}_u \hat{E}_k) - \Delta t_u \vec{\nabla}_u \hat{E}_k$$

with Δt_p, Δt_u fixed time steps. The evolution equations are:

$$\frac{\partial \hat{E}_k}{\partial p_{n,l}} = \left(\int_\Omega \delta(\phi_n \circ \psi_n).\langle\vec{\nabla}\phi_n \circ \psi_n, \frac{\partial \mathcal{G}_n}{\partial p_{n,l}} \circ \mathcal{L}\rangle.f_n\right) + \mu_k.Q_{n,l}$$

$$\vec{\nabla}_u \hat{E}_k = K_\sigma * \left\{\sum_{n=1}^{N} \delta(\phi_n \circ \psi_n).f_n.(d\mathcal{G}_n)^t \vec{\nabla}\phi_n \circ \psi_n\right\} + \lambda\mathbf{u}$$

with:

$$Q_{n,l} = \sum_{\substack{1<j\le N \\ j\neq n}} C_{n,j} \int_\Omega H(\phi_j \circ \mathcal{G}_j).\delta(\phi_n \circ \mathcal{G}_n).\langle\vec{\nabla}\phi_n \circ \mathcal{G}_n, \frac{\partial \mathcal{G}_n}{\partial p_{n,l}}\rangle$$

As in [1], the equations allow us to compute the terms $\vec{\nabla}\phi_n \circ \psi_n$ and $\phi_n \circ \psi_n$ only near their zero level. By defining ϕ_n as distance functions we can compute them in an efficient coarse-to-fine approach using octrees (refer to [1] for details).

3. APPLICATION TO CT ORGAN SEGMENTATION

To evaluate our algorithm we propose to segment simultaneously several organs (the liver, the heart, the two kidneys, the spleen and the gallbladder) in 3D CT images.

3.1. Workflow and Parameterization

A key feature of our framework is its flexibility. It can be easily adapted to users' requirements. For this application, we perform the segmentation in an efficient two-steps coarse-to-fine fashion following the approach of [11] for liver segmentation. Forces are re-computed after each optimization step, using the resulting contours from the previous step. In the coarse step we initialize transformations $\psi_n = \mathcal{G}_n \circ \mathcal{L}$, with $\mathcal{G}_n$ as similarities, from the localization step and optimize them. Image forces rely equally on region and edge terms ($\alpha = 0.5$ in Eq.3). The second, refinement step aims at reaching the edges of the organs. The transformation optimized is here only local and non-rigid ($\psi_n = \mathcal{L}$) and image forces now mainly rely on edges ($\alpha = 0.8$).

3.2. Database and Implementation

Our database includes 100 CT volumes from different patients, with varied fields of view, body shapes, resolution and use or not of contrast agents. Slice and inter-slice resolutions range from 0.5 to 1 mm and from 0.5 to 3 mm, respectively. We split the database in 50 volumes for training (localization part and parameters tuning) and 50 for testing. The organs (liver, kidneys, spleen, gallbladder and heart) were segmented manually by an expert for training and evaluation purposes. Our method is implemented in C++ and running times are given for a machine with two 2.3 GHz cores and 8 Gb RAM.

3.3. Results

The table of Fig. 4 reports computation times and quantitative accuracy results for the liver, kidneys, spleen and gallbladder. The heart is omitted from the quantitative results, as its visibility is highly variable in our database. It remains however useful within the segmentation process, e.g. to constrain the liver contours. Figures 1 and 4 give examples of the obtained results. For each organ, the accuracy increases after each step. Eventually, we obtain results of the order of the best reported methods (e.g., 2.9 and 1.35mm average for the liver and kidneys in [3]). Our worst results are obtained for the gallbladder, an organ with high shape and appearance variability. High localization errors largely impede subsequent optimization. Our experiments also highlighted

	Localization		Coarse step		Refined step	
	MD (mm)	Dice (%)	MD (mm)	Dice (%)	MD (mm)	Dice (%)
Liver	21.2	59	4.1	93	2.3 ± 1 (2)	94 ± 3 (94)
Kidneys	7.6	64	5.3	86	1.8 ± 4 (0.6)	92 ± 16 (96)
Spleen	10.3	58	5.6	80	2.6 ± 3 (2)	87 ± 15 (92)
Gallbladder	9.1	29	7.9	32	7.5 ± 6 (5)	37 ± 36 (35)
Time (sec.)	7 ± 2 (6)		16 ± 6 (13)		11 ± 2 (10)	

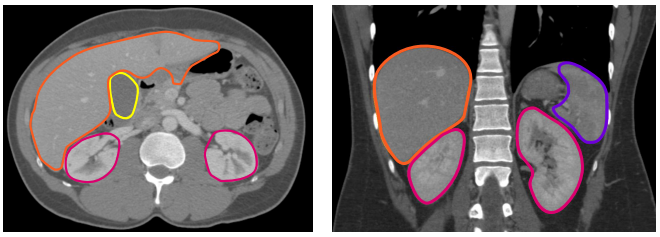

Fig. 4. Left: mean distances and dice coefficient ($\pm$ standard deviation (median)) to ground truth results and computational time after each step. Examples of results in axial (middle) and sagittal places (right) (liver, kidneys, spleen and gallbaldder).

the benefit of the non-overlapping constraint on segmentation accuracy (e.g. 4mm mean distance for the kidneys without the constraint). Overall, we believe that these results are very promising, given that we kept our method as generic as possible. In particular, we used the same forces for each organ and did not perform advanced parameter tuning. The entire pipeline runs in about 30s on average. Such runtimes remain compatible with most clinical workflows.

4. CONCLUSION AND PERSPECTIVES

We propose a fast, automatic and flexible framework for the simultaneous segmentation of multiple objects from 2D or 3D images. It extends previous work on implicit template deformation [1] to multiple objects with non-overlapping constraints. We show the potential of our approach on a challenging application, the segmentation of abdominal organs from 3D CT data. We obtain state-of-the-art accuracy results for low runtime (under 1min) while keeping our algorithm as generic as possible. We believe parameter tuning could further improve the accuracy of the method. One could for instance incorporate organ-specific image forces learned with discriminative classifiers, as in [10]. We emphasize the genericity and flexibility of our approach. Our contributions for multi-object segmentation integrate seamlessly within the template deformation framework of [1] and can easily be combined with refinements such as user constraints for interactive corrections [1] or region-specific *tagged* forces [10]. Finally, we intend to explore applications to other modalities such as MRI or ultrasound data and other anatomies, such as brain, cardiac or pelvic structures.

5. REFERENCES

[1] B. Mory, O. Somphone, R. Prevost, and R. Ardon, "Real-time 3D image segmentation by user-constrained template deformation," in *MICCAI*, vol. 7510 of *LNCS*, pp. 561–568. 2012.

[2] R. Wolz, C. Chu, K. Misawa, K. Mori, and D. Rueckert, "Multi-organ abdominal CT segmentation using hierarchically weighted subject-specific atlases," in *MICCAI*, vol. 7510 of *LNCS*, pp. 10–17. 2012.

[3] T. Kohlberger, M. Sofka, J. Zhang, N. Birkbeck, J. Wetzl, J. Kaftan, J. Declerck, and S. Zhou, "Automatic multi-organ segmentation using learning-based segmentation and level set optimization," in *MICCAI*, vol. 6893 of *LNCS*, pp. 338–345. 2011.

[4] N. Lay, N. Birkbeck, J. Zhang, and S. Zhou, "Rapid multi-organ segmentation using context integration and discriminative models," in *IPMI*, vol. 7917 of *LNCS*, pp. 450–462. 2013.

[5] B. Glocker, O. Pauly, E. Konukoglu, and A. Criminisi, "Joint classification-regression forests for spatially structured multi-object segmentation," in *ECCV*, 2012, vol. IV, pp. 870–881.

[6] R. Gauriau, R. Cuingnet, D. Lesage, and I. Bloch, "Multi-organ localization combining global-to-local regression and confidence maps," in *MICCAI*, 2014, vol. 8675 of *LNCS*, pp. 337–344.

[7] B. Mory, *Interactive Segmentation of 3D Medical Images with Implicit Surfaces*, Ph.D. thesis, EPFL, 2011.

[8] R. Prevost, *Variational methods for model-based image segmentation - application in medical imaging*, Ph.D. thesis, Université Paris-Dauphine, CEREMADE, 2013.

[9] R. Kimmel and A. M. Bruckstein, "Regularized Laplacian zero crossings as optimal edge integrators," *International Journal of Computer Vision*, vol. 53, no. 3, pp. 225–243, 2003.

[10] R. Prevost, R. Cuingnet, B. Mory, L. D. Cohen, and R. Ardon, "Tagged template deformation," in *MICCAI*, vol. 8673 of *LNCS*, pp. 674–681. 2014.

[11] R. Gauriau, R. Cuingnet, R. Prevost, B. Mory, R. Ardon, D. Lesage, and I. Bloch, "A generic, robust and fully-automatic workflow for 3D CT liver segmentation," in *Abdominal Imaging. Computation and Clinical Applications (MICCAI workshop)*, vol. 8198 of *LNCS*, pp. 241–250. 2013.